

This is an electronic reprint of the original article. This reprint may differ from the original in pagination and typographic detail.

Analysis of Nanowire pn-Junction with Combined Current–Voltage, Electron-Beam-Induced Current, Cathodoluminescence, and Electron Holography Characterization

Anttu, Nicklas; Fiordaliso, Elisabetta Maria; Garcia, José Cano; Vescovi, Giuliano; Lindgren, David

Published in:
Micromachines

DOI:
[10.3390/mi15010157](https://doi.org/10.3390/mi15010157)

Published: 01/01/2024

Document Version
Final published version

Document License
CC BY

[Link to publication](#)

Please cite the original version:

Anttu, N., Fiordaliso, E. M., Garcia, J. C., Vescovi, G., & Lindgren, D. (2024). Analysis of Nanowire pn-Junction with Combined Current–Voltage, Electron-Beam-Induced Current, Cathodoluminescence, and Electron Holography Characterization. *Micromachines*, 15, Article 157. <https://doi.org/10.3390/mi15010157>

General rights

Copyright and moral rights for the publications made accessible in the public portal are retained by the authors and/or other copyright owners and it is a condition of accessing publications that users recognise and abide by the legal requirements associated with these rights.

Take down policy

If you believe that this document breaches copyright please contact us providing details, and we will remove access to the work immediately and investigate your claim.



Article

Analysis of Nanowire pn-Junction with Combined Current–Voltage, Electron-Beam-Induced Current, Cathodoluminescence, and Electron Holography Characterization

Nicklas Anttu, Elisabetta Maria Fiordaliso, José Cano Garcia, Giuliano Vescovi and David Lindgren

Special Issue

III-V Optoelectronics and Semiconductor Process Technology

Edited by

Dr. Hsin-Chu Chen, Prof. Dr. Hao-Chung Kuo and Prof. Dr. Yi-Jen Chiu





Article

Analysis of Nanowire pn-Junction with Combined Current–Voltage, Electron-Beam-Induced Current, Cathodoluminescence, and Electron Holography Characterization

Nicklas Anttu ^{1,*} , Elisabetta Maria Fiordaliso ², José Cano Garcia ³, Giuliano Vescovi ³ and David Lindgren ³

¹ Physics, Faculty of Science and Engineering, Åbo Akademi University, FI-20500 Turku, Finland

² National Centre for Nano Fabrication and Characterization, Technical University of Denmark, 2800 Kongens Lyngby, Denmark

³ Sol Voltaics AB, 223 63 Lund, Sweden

* Correspondence: nicklas.anttu@abo.fi

Abstract: We present the characterization of a pn-junction GaAs nanowire. For the characterization, current–voltage, electron-beam-induced current, cathodoluminescence, and electron holography measurements are used. We show that by combining information from these four methods, in combination with drift-diffusion modelling, we obtain a detailed picture of how the nanowire pn-junction is configured and how the recombination lifetime varies axially in the nanowire. We find (i) a constant doping concentration and 600 ps recombination lifetime in the n segment at the top part of the nanowire; (ii) a 200–300 nm long gradient in the p doping next to the pn-junction; and (iii) a strong gradient in the recombination lifetime on the p side, with 600 ps lifetime at the pn-junction, which drops to 10 ps at the bottom of the p segment closest to the substrate. We recommend such complementary characterization with multiple methods for nanowire-based optoelectronic devices.

Keywords: III–V semiconductor nanowire; electron-beam-induced current; cathodoluminescence; current–voltage characterization; electron holography; drift-diffusion modelling



Citation: Anttu, N.; Fiordaliso, E.M.; Garcia, J.C.; Vescovi, G.; Lindgren, D. Analysis of Nanowire pn-Junction with Combined Current–Voltage, Electron-Beam-Induced Current, Cathodoluminescence, and Electron Holography Characterization. *Micromachines* **2024**, *15*, 157. <https://doi.org/10.3390/mi15010157>

Academic Editors: Hao-Chung Kuo, Hsin-Chu Chen and Yi-Jen Chiu

Received: 29 November 2023

Revised: 10 January 2024

Accepted: 17 January 2024

Published: 20 January 2024



Copyright: © 2024 by the authors. Licensee MDPI, Basel, Switzerland. This article is an open access article distributed under the terms and conditions of the Creative Commons Attribution (CC BY) license (<https://creativecommons.org/licenses/by/4.0/>).

1. Introduction

III–V semiconductor nanowires [1–5] have received considerable interest for optoelectronic applications such as in solar cells [6–12], photodetectors [13,14], and light-emitting diodes [15]. In such applications, different regions of the nanowire are intentionally doped with donors and acceptors to induce n- or p-type doping [16,17]. The configuration of the n-type and p-type regions, together with the recombination lifetime of excess charge carriers, affects the optoelectronic response of the nanowire [18,19], as observed for example with current–voltage (IV) measurements on the nanowires. However, in the bottom-up fabrication of nanowires, non-intentional gradients in both doping profile and recombination lifetime can show up [20]. Therefore, assessment of these parameters and their possible spatial variation within the nanowire is of great interest.

Electron-beam-induced current (EBIC) measurements have been used to understand the spatially varying probability for extraction of photogenerated charge carriers in nanowires [20–25]. With electron holography, it has been possible to obtain the electrostatic potential gradient inside nanowires [26–28]. Cathodoluminescence (CL) measurements can be used for assessing doping concentration and luminescence properties in nanowires [29–31].

Here, we perform IV, EBIC, CL, and electron holography measurements on GaAs nanowires that have a pn-junction. We show that by combining information from these four methods, in combination with drift-diffusion modelling, we obtain a detailed picture of how the nanowire pn-junction is configured and how the recombination lifetime varies within the nanowire.

We recommend such complementary characterization with multiple methods for nanowire-based optoelectronic devices. In our opinion, none of the methods by themselves provide sufficient information for efficient development of devices.

2. Materials and Methods

2.1. Nanowire Growth

The GaAs nanowires are grown using metalorganic vapor-phase epitaxy (MOVPE), in a similar manner as in Ref. [32]. The growth substrate is a p-type GaAs substrate, with approximately 10^{16} cm^{-3} doping concentration, which is patterned with a 500 nm period, square array of Au catalyst particles. In the growth design for the current study, the nanowire growth is intended to switch from p-type dopant to n-type dopant at a height of 1250 nm of a 2500 nm long GaAs nanowire (note that in Ref. [32], in contrast, a deliberate i-region was aimed for, to induce an n-i-p diode configuration). The GaAs core is approximately 160 nm in diameter, and there is an $\text{Al}_x\text{Ga}_{1-x}\text{As}$ high-bandgap passivation shell layer of approximately $x = 0.80$ and 30–50 nm in thickness. For additional details of the nanowire growth, see Section S1 in the Supplementary Materials. See Figure 1a for a scanning electron microscope (SEM) image of the as-grown nanowires.

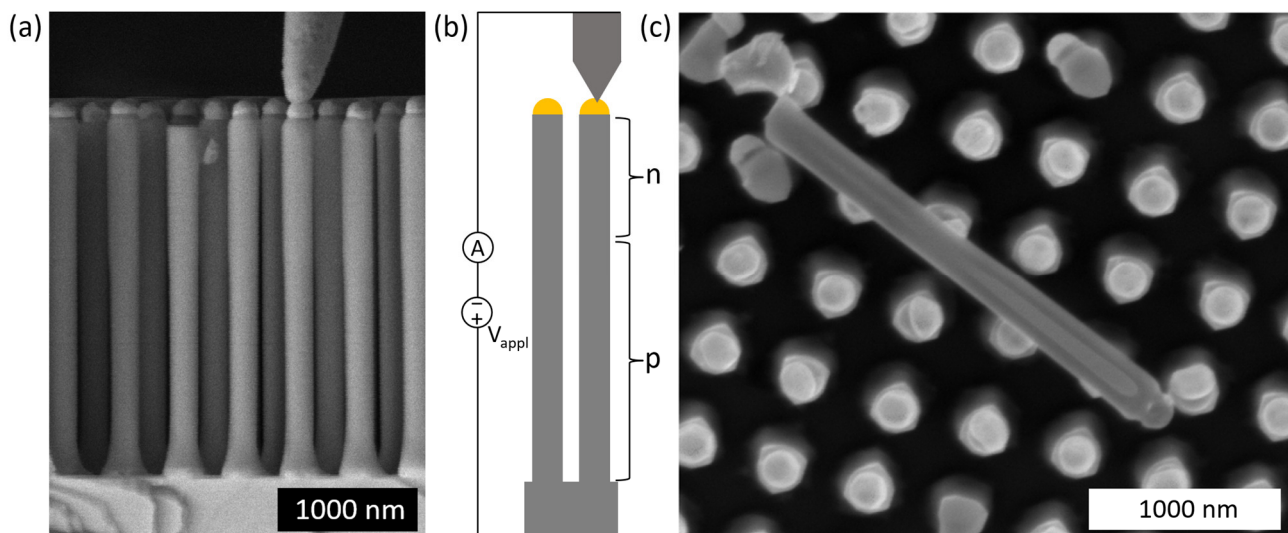


Figure 1. (a) SEM image in side-view of as-grown GaAs nanowires with the nanoprobe at the top of a nanowire and the GaAs substrate below the nanowires. (b) Schematic of the nanoprobe contacting, which is used in IV, EBIC, and CL measurements. Here, n and p indicate the n and p regions. (c) SEM image of a GaAs nanowire left lying flat on the growth substrate when shaving off the nanowires for transfer to TEM grid for electron holography measurements.

2.2. IV and EBIC Measurements with Nanoprobe Contacting

We perform IV and EBIC characterization of a single as-grown GaAs nanowire using a nanoprobe (PS4 Prober Shuttle, Kleindiek Nanotechnik, Reutlingen, Germany) inside an SEM (SU8010, Hitachi High-Tech Corporation, Tokyo, Japan) to contact the Au particle at the top of the nanowire (see Figure 1b for a schematic). The same combination of SEM and nanoprobe is used as in Ref. [32]—see Ref. [20] for an example of similar nanoprobe characterization of InP nanowires. The substrate is used as the second contact. For the IV curves, external bias V_{appl} is applied and the current is measured. For EBIC measurements, the external bias is kept at $V_{\text{appl}} = 0 \text{ V}$, the electron beam in the SEM is scanned in a point-like manner over the nanowire, and for each measurement point, the current in the external circuit is recorded.

2.3. CL Characterization

The CL characterization is performed with a hyperspectral CL imaging system (SPARC, Delmic, Delft, The Netherlands) installed to the same SEM as that for IV and EBIC measurements in Section 2.2 above (see Ref. [29] for details of the setup). For this study, the CL measurements are conducted on a single as-grown nanowire, after contacting the nanowire with the above nanoprobe and keeping the external circuit in short-circuit condition (that is, at $V_{\text{appl}} = 0$ externally). With the short-circuit condition, we minimize the contribution to CL from excess charge carriers that, after diffusing to the pn-junction, bias the pn-junction, leading to luminescence from the junction region. For the CL spectrum at the middle of the p side and n side, respectively, see Figure S1 in the Supplementary Materials.

2.4. Electron Holography Characterization

Off-axis electron holography is a powerful method for dopant assessment in nanostructures [26]. Electron holography is a transmission electron microscopy (TEM) technique that measures a spatially resolved phase difference, $\Delta\phi$, using interference between electrons that pass through the specimen (object wave) and electrons that pass through the vacuum (reference wave). $\Delta\phi$ is related to the crystal potential, or mean inner potential (MIP) $V(x, y, z)$, according to [26]

$$\Delta\phi = CE \int_0^t V(x, y, z) dz$$

where CE is a microscope acceleration voltage-dependent constant, and t is the specimen thickness. CE is equal to 8.64×10^6 rad/Vm for a TEM operating at 120 kV.

Here, nanowires are transferred from their substrate to a TEM grid after scratching the surface gently with a tweezer. Holograms are recorded using an FEI Titan 80-300ST field emission gun TEM (ThermoFischer, Waltham, Washington, DC, USA), operating at 120 kV and equipped with a rotatable Möllenstedt biprism.

2.5. Drift-Diffusion Modelling

To support the analysis of the characterization results, we perform drift-diffusion modelling for the electron-hole transport. The numerical solving of the drift-diffusion equations is performed with the Semiconductor Module in Comsol Multiphysics. Due to the axial configuration of the pn-diode, we use a one-dimensional (1D) approximation of the nanowire, such that only the axial position enters our simulations. For details and validity of the 1D model, see Ref. [19].

In the modelling, we assume a temperature of $T = 300$ K, use Fermi-Dirac statistics for the carrier concentrations, and, for simplicity, we do not take into account possible carrier-concentration-induced bandgap narrowing in the simulations. Furthermore, for GaAs, we assume a bandgap of 1.424 eV [33], effective conduction band density of states of $4.7 \times 10^{17} \text{ cm}^{-3}$ [16], and effective valence band density of states of $9.0 \times 10^{18} \text{ cm}^{-3}$ [16].

We perform two types of drift-diffusion modelling. (1) In IV modelling, we apply an external voltage V_{appl} over the top and the bottom of the nanowire and record the current that flows through the nanowire. Furthermore, at zero external bias, we obtain the modelled built-in voltage, which can be compared to the built-in voltage extracted from electron holography. (2) In spatially-resolved internal quantum efficiency (SIQE) modelling, we keep the external bias at zero voltage, include a localized excess carrier generation source inside the nanowire, and record how many charge carriers are extracted as current [18]. We define SIQE as the ratio of extracted charge carriers to the amount of excess carriers injected by the local generation source. Then, SIQE can be compared to the measured EBIC curve, also quantitatively, assuming that the peak of the measured EBIC curve corresponds to 100% extraction of the electron-beam-induced excess charge carriers.

2.5.1. Mobility

In our drift-diffusion modelling, we take into account the doping-induced modification of the charge-carrier mobility with the empirical model in Ref. [34], assuming the above $T = 300$ K. Then, we have $\mu_{e/h,n/p} = \mu_{\min,e/h} + \frac{\mu_{\max,e/h} - \mu_{\min,e/h}}{1 + (N_{n/p}/N_{ref,e/h})^{\lambda_{e/h}}}$ where e/h denotes electrons/holes and n/p denotes the n or p region, with parameters from Ref. [34], as summarized in Table 1. For the n region, we use $N_n = N_D$, and for the p region, $N_p = N_A$.

Table 1. Mobility parameters for GaAs from Ref. [34].

Quantity	Value
$N_{ref,e}$	$6.0 \times 10^{16} \text{ cm}^{-3}$
$N_{ref,h}$	$1.48 \times 10^{17} \text{ cm}^{-3}$
λ_e	0.394
λ_h	0.38
$\mu_{\min,e}$	$500 \text{ cm}^2/\text{Vs}$
$\mu_{\min,h}$	$20 \text{ cm}^2/\text{Vs}$
$\mu_{\max,e}$	$9400 \text{ cm}^2/\text{Vs}$
$\mu_{\max,h}$	$491.5 \text{ cm}^2/\text{Vs}$

2.5.2. Recombination

We assume that non-radiative recombination dominates the overall recombination. This assumption is supported by the doping values that we extract below, which are low enough, implying that Auger recombination is negligible, and the non-radiative recombination parameter in our modelling which needs to be set so high that it indicates that radiative recombination is negligible. See Ref. [35] for additional details of such an assumption of non-radiative recombination dominating overall recombination in nanowires. In our modelling, we use a Shockley-Read-Hall-type non-radiative recombination mechanism with a single trap level (whose energy is assumed to coincide with the Fermi energy in an intrinsic semiconductor), with the same lifetime τ_{rec} for electrons and holes. In our 1D model, τ_{rec} can show dependence on the axial position, and both surface and bulk recombination are included through τ_{rec} —see Equation (3) in Ref. [35] for details of how surface recombination enters through this recombination lifetime.

3. Results and Discussion

We start by presenting the characterization results in Sections 3.1–3.5. After that, in Section 3.6, we use the drift-diffusion model of the nanowire for an additional analysis of the characterization results to extract further quantitative information about the configuration of the nanowire pn-junction and recombination lifetime.

3.1. IV Measurements

The IV curve for a nanowire is shown in Figure 2. The behavior is typical of a diode. We find that this diode opens up at approximately 0.7 V, with an exponential increase in the current with increasing voltage after that, until series resistance sets in at approximately 1.1 V. Therefore, it is the $0.7 < V_{\text{appl}} < 1.1$ V range that reveals the clearest facts about the operation of this nanowire diode.

3.2. Electron Holography

The potential profile extracted from electron holography is shown in Figure 3a. Here, the pn-junction can be seen as the rapid variation in the potential profile at $z \approx 1600$ nm. The slope of the potential profile is proportional to the electric-drift field, which aids in the separation of charge carriers, and which is thus expected to lead to high EBIC values. Indeed, the location of the pn-junction as indicated by the potential profile coincides well with the region where the EBIC profile peaks (as discussed below in Section 3.3).

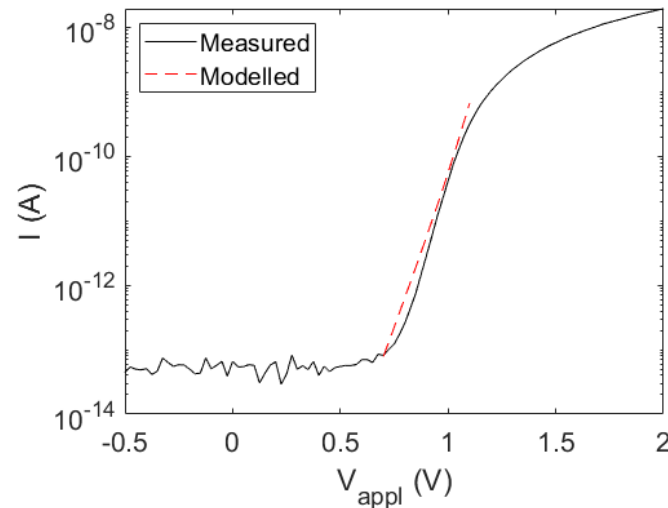


Figure 2. Measured (solid line) and modelled (dashed line) current vs. voltage for a nanowire (see Figure 1b for a schematic). At $V_{\text{appl}} > 1.1$ V, we see the onset of series resistance in the order of $30 \text{ M}\Omega$. Note that there is a very minor offset in the zero value of the measured current.

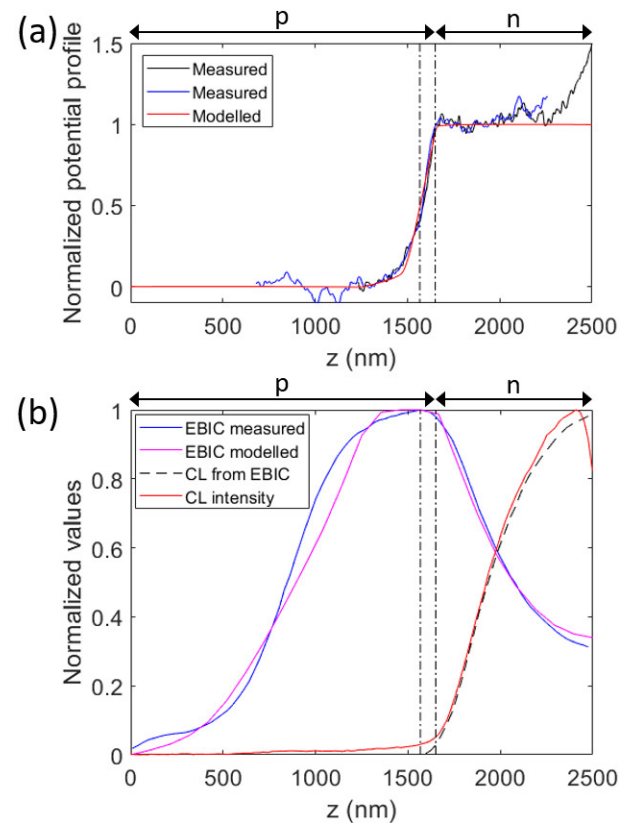


Figure 3. (a) Normalized electron potential profile extracted from electron holography as a function of axial position z in a nanowire. The large increase in the potential at $z \approx 1600$ nm is assigned to the pn-junction. The second line scan, with smaller z values, is included to show the continuation of the profile away from the pn-junction. Here also, normalized values for the potential from our drift-diffusion model are shown, for $V_{\text{appl}} = 0$, that is, zero applied voltage. The measured spectra are shifted such that each of their mean value for $z < 1250$ nm is equal to zero, and after that they are normalized such that each of their mean values for $1700 < z < 2000$ nm are equal to one. The modelled potential profile is shifted such that the value at $z = 0$ is at zero, before normalizing to the maximum value. (b) Measured and modelled EBIC and measured CL intensity as a function of the axial position in the nanowire, with $z = 0$ indicating the bottom of the nanowire at the substrate

surface and $z = z_{\max} = 2500$ nm at the top of the GaAs core of the nanowire. The CL intensity is integrated for photon energies in the 1.12 to 1.85 eV range. The EBIC peaks at $z = z_{\text{peak}} = 1567$ nm. The dashed line shows values from a model that corresponds to the assumption of diffusion-dominated transport and constant recombination lifetime in the n region, with perfect FSB at the top of the nanowire (in which case a direct relation exists between the CL intensity and EBIC signal—see the main text for details). The dashed-dotted vertical lines are placed at $z = 1567$ nm and at $z = 1650$ nm to guide the eye. The arrows with p and n mark the p side and n side.

We note that the increase in the potential profile appears to start at $z \approx 1250$ nm, which is the position according to the growth design where the dopant precursor was changed from the p type to n type. The potential profile returns to a flat profile at $z \approx 1650$ nm (except for the increase at the very top of the nanowire, which we assign to a thin, axial AlGaAs segment, originating from the AlGaAs growth used for the radial surface passivation), indicating that the dopant concentration is constant on the n side for larger z values than this. In the continuation, when we refer to the n side, we refer to the region with $z > 1650$ nm.

3.3. EBIC Measurements

The (normalized) EBIC profile is shown in Figure 3b. The peak of the EBIC occurs at a height of approximately 1570 nm from the substrate surface. For a sharp pn-junction, with constant p and n doping around the junction and a constant lifetime, we would expect exponential decay, with the diffusion length, of the EBIC signal being away from the junction (see Section 3.2.1 in Ref. [35] for the effect of pn-junction design on modelled SIQE, which is probed using EBIC measurements). Our results indicate that our nanowire does not show such a simple, abrupt pn-junction. We believe that such a gradient in doping occurs due to the reservoir effect for dopants in the Au catalyst particle [36].

The rather high value of 0.32 for the EBIC at the top of the nanowire indicates that a front-surface barrier (FSB) is present, which prevents the electron-beam-induced excess minority carriers (that is, holes in the top n region) from reaching the top metal contact where they would recombine efficiently (which would lead to $\text{EBIC} \rightarrow 0$ at the top of the nanowire, see Section 3.2 in Ref. [35] for details)—in other words, the FSB functions as an electron-selective contact. This FSB is probably due to the thin axial segment of the high-bandgap AlGaAs that was used for the surface passivation; effects from such an axial AlGaAs segment are visible also in the electron holography measurements, as discussed above. We expect the axial AlGaAs segment on top of the GaAs n region to be n doped due to memory effect of dopants in the Au catalyst particle during growth, in which case the conduction band of the AlGaAs and GaAs regions align, while the bandgap difference causes an efficient hole-blocking effect (see Section 3.5 in Ref. [18] for further details).

Since the EBIC profile does not decay exponentially for $z < 1570$ nm, we have indication that the p segment shows variation in the axial direction in N_A and/or τ_{rec} .

3.4. Dependence of CL Intensity along Nanowire Axis and Comparison to EBIC Signal

The CL intensity as a function of axial position is shown in Figure 3b. On the n side, the CL signal increases as the EBIC signal decreases when moving away from the pn-junction. This behavior matches the expectation that the diffusion of excess minority carriers to the pn-junction, to which the EBIC signal is proportional, and the recombination, to which the CL signal is proportional, are competing processes (in other words, (i) a high EBIC signal leads to fewer excess minority carriers that are not extracted as an external current, and (ii) those non-extracted excess minority carriers are the ones leading to net recombination that is probed by CL. Therefore, a high EBIC signal is expected to result in a low CL signal and vice versa). If we assume a diffusion-dominated transport and constant recombination lifetime in the n region, with perfect FSB at the top of the nanowire, we can write a straight-forward quantitative relationship between the CL signal and EBIC

signal. In that case, the CL signal is found using $1 - \frac{EBIC(z) - EBIC(z_{\max})}{EBIC(z_{\text{peak}}) - EBIC(z_{\max})}$. The dashed line in Figure 3b shows values from that model for the CL signal. Indeed, we find good agreement between the measured CL intensity profile and this model.

However, on the p side, when moving away from the pn-junction, both the EBIC and CL signal drop. Thus, here, a similar simple connection between EBIC and CL intensity profiles does not show up as on the n side. Again, we thus have an indication that the configuration, in terms of recombination-lifetime profile and/or doping profile in the axial direction, of the p side is more complicated than on the n side.

3.5. Extraction of Doping Concentration from CL Measurements

From the CL characterization, we can extract doping concentration with a model that relates characteristics of the CL spectrum to doping concentrations. Here, the doping concentration on the respective sides of the pn-junction was estimated using the full width at half maximum (FWHM) of the bandgap-related-peak E_{FWHM} from room-temperature short-circuited hyperspectral CL measurements, using $p = \left(\frac{E_{\text{FWHM}} - B}{1.68 \cdot 10^{-8} \text{ eV}} \right)^3 \text{ cm}^{-3}$ and $n = \left(\frac{E_{\text{FWHM}} - B}{3.4 \cdot 10^{-14} \text{ eV}} \right)^2 \text{ cm}^{-3}$ for p- and n-type doping, respectively. Refs. [37,38] describe similar estimation equations. This model is based on CL data of p-type and n-type bulk substrate reference samples of various and known concentrations. Typically, a model based on FWHM is given as a simple power law using a scaling factor, but, in our case, a broadening parameter has been used, since we aimed for a general model that would take into account the effects from the quality of surface passivation. That is, our model is intended to enable the estimation of doping concentrations for varying quality of the surface passivation. For well-passivated nanowires (such as in our case with a thick, high-bandgap AlGaAs passivation shell), the broadening parameter B becomes 37 meV from the fitting to reference samples (note that this value is close to the typical FWHM value for intrinsic bulk GaAs [39], and thus the model is intended only for noticeably doped samples, since for low-doped samples approaching the intrinsic linewidth, the model will provide a very low, or even unphysical, doping concentration). With poorer passivation, surface states will affect the linewidth, and the broadening term will increase. The full calibration approach goes beyond the scope of this paper and is planned for a separate publication.

Then, with the measured E_{FWHM} , we find on the n side a rather constant $N_D \approx 2.4 \times 10^{18} \text{ cm}^{-3}$, with a mild decrease to $1.9 \times 10^{18} \text{ cm}^{-3}$ at $z = 1650 \text{ nm}$ (see Figure S2 in the Supplementary Materials). On the p side, we find a rather constant N_A with the lowest value of $9.3 \times 10^{18} \text{ cm}^{-3}$ and the highest value of $1.2 \times 10^{19} \text{ cm}^{-3}$ (see Figure S2 in the Supplementary Materials). Extraction of the doping profile within the junction region from the CL FWHM is not trivial due to the depletion of free carriers and the very strong drift of excess charge carriers in that region.

3.6. Analysis of Characterization Results with the Help of Drift-Diffusion Model

For further analyses of the characterization results, we have built a drift-diffusion model for the nanowire. As a starting point, we will use the following characteristics extracted from the measurements above:

1. We assume a transition to the n type region at $z = 1650 \text{ nm}$, with $N_D(z)$ having the rather constant value of $2.4 \times 10^{18} \text{ cm}^{-3}$, with exact values provided from the CL characterization (see Figure S2 in the Supplementary Materials). For this n region, we assume a constant τ_{rec} . This assumption of a constant τ_{rec} is motivated by the good agreement in Section 3.2 between the CL intensity profile and the modelled values from the EBIC profile that also used the assumption of a constant N_D and τ_{rec} on the n side (producing the dashed line in Figure 3b).
2. We assume an FSB at the top of the nanowire, as indicated by the EBIC profile which stays at a value of >0.3 there, instead of dropping to zero as expected if no FSB was present (as discussed in Section 3.2). We include this FSB in the model through an

n-doped AlGaAs segment at $z > 2500$ nm before the top contact, which is placed at $z = 2600$ nm.

3. For the p-type region, we use the $N_A(z)$ extracted from the CL measurements (see Figure S2 in the Supplementary Materials) for $0 < z < 1250$ nm. This value of $z = 1250$ nm is motivated by the growth recipe described in Section 2.1 where the dopant is switched from p type to n type nominally at this value for z . Furthermore, the potential profile from the electron holography starts to vary from a flat profile at this $z = 1250$ nm (Figure 3a). Importantly, if we use the N_A extracted from CL also for $1250 < z < 1500$ nm, we are unable to reproduce the electron holography and the EBIC profiles (see Figures S3 and S4 in the Supplementary Materials).

Thus, in our drift-diffusion model for the nanowire, we have as unknown parameters (i) τ_{rec} in the n region, and this τ_{rec} should be independent of z , (ii) values for $\tau_{\text{rec}}(z)$ for $z < 1650$ nm, and (iii) values for $N_A(z)$ for $1250 < z < 1650$ nm. These parameters should be tuned in such a way that we can recreate the characterization results from Sections 3.1–3.5.

We start by varying the doping profile for $1250 < z < 1650$ nm in order to recreate the potential profile measured with electron holography in Figure 3a. Importantly, the modelled potential profile is not dependent on $\tau_{\text{rec}}(z)$, since we model the potential profile at $V_{\text{appl}} = 0$. Here, it is important to note that the measured potential profile in Figure 3a provides for us a built-in voltage for the pn-junction of approximately 1.0 V (as obtained from the non-normalized measurement data underlying the normalized data shown in Figure 3a). However, such a low built-in voltage corresponds, for example, to $N_A \approx 1 \times 10^{15} \text{ cm}^{-3}$ and $N_D \approx 1 \times 10^{15} \text{ cm}^{-3}$ in GaAs, as obtained from semiconductor equations [16]. Thus, it appears that the built-in voltage extracted from the measurements in Figure 3a is noticeably lower than expected. Similar, lower-than-expected values for the built-in voltage for nanowires from electron holography have been seen also in other studies [26]. Therefore, when comparing measured and modelled potential profiles, we use normalized profiles.

For the doping gradient profile, we chose to use erf, the error function. Then, since we have from the CL measurements N_A at the beginning of the pn-junction, we have just a scaling parameter L_{erf} for the argument to the erf to adjust. With $N_A(z) = N_A(z_0)(1 - \text{erf}[(z - z_0)/L_{\text{erf}}])$ for $1250 < z < 1650$ nm, with $z_0 = 1250$ nm as the start of the graded region, we find rather good agreement between the measured and modelled potential profile with $L_{\text{erf}} = 130$ nm (Figure 3a).

Now that we have fixed the doping profile in the model, we turn to consider the remaining free parameter, that is, the possibly z -dependent $\tau_{\text{rec}}(z)$ for $z < 1650$ nm and the constant value for τ_{rec} for $z > 1650$ nm.

We proceed as follows: (i) on the n side, we find that $\tau_{\text{rec}} = 600$ ps provides good agreement between measured and modelled EBIC profiles (Figure 3b). (ii) Next, we assume first a position-independent τ_{rec} also for the bottom part of the nanowire, with the aim of finding a value that reproduces in the modelling the measured IV curve. During this testing, we found that a value of $\tau_{\text{rec}} = 600$ ps also in the pn-junction area (where the recombination in forward bias occurs), provides good agreement between measured and modelled IV curves. (iii) To allow for possible position dependence in τ_{rec} for $z < 1250$ nm, we used this constant $\tau_{\text{rec}} = 600$ ps for $z > 1250$ nm, since the recombination in the forward direction was found to occur predominantly in the $1250 < z < 1650$ nm region (see Figure S6 in Supplementary Materials). In this way, we allow for a possible gradient in τ_{rec} for $z < 1250$ nm without deteriorating the good agreement between the modelled and measured IV curves found in (ii). First, when we attempted to use a constant τ_{rec} for $z < 1250$ nm, we did not find good agreement with the measured EBIC profile (see Figure S5 in the Supplementary Materials). However, with $\tau_{\text{rec}} = 10$ ps for $z < 500$ nm and a linear increase in τ_{rec} from 10 ps at $z = 500$ nm to 600 ps at $z = 1250$ nm, we find rather good agreement between the measured and modeled EBIC profiles also on the p side (see Figure 3b). The resulting good agreement between the measured and modelled IV curves is shown in Figure 2. The extracted values for $N_A(z)$, $N_D(z)$, and $\tau_{\text{rec}}(z)$ are shown in Figure 4.

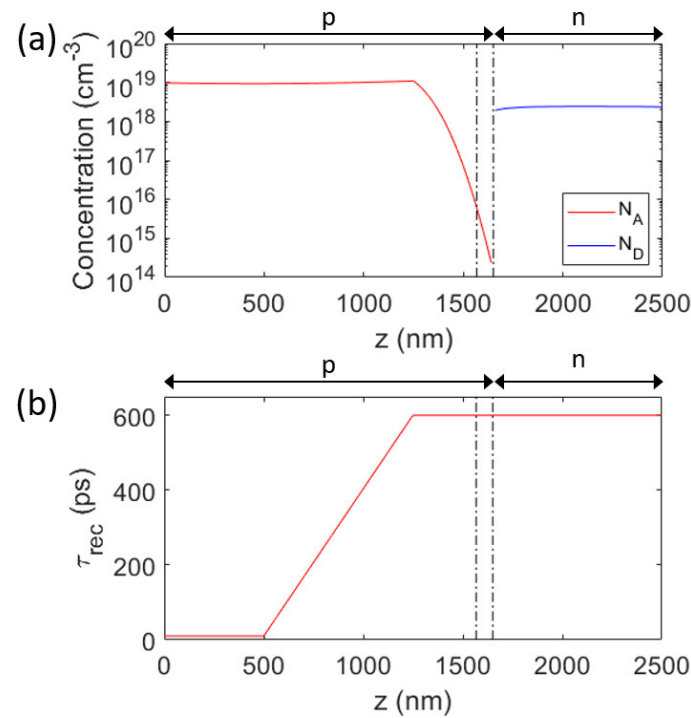


Figure 4. (a) The $N_A(z)$ and $N_D(z)$ and (b) the $\tau_{\text{rec}}(z)$ used in the drift-diffusion model. Here, $\tau_{\text{rec}} = 10$ ps for $z < 500$ nm. The dashed–dotted vertical lines are placed at $z = 1567$ nm and at $z = 1650$ nm to guide the eye. The arrows with p and n mark the p side and n side.

4. Conclusions

By combining the IV, EBIC, CL, and electron holography measurements with the drift-diffusion model of the nanowire, we could reveal a plausible configuration for the nanowire (Figure 4). From CL measurements, we obtained estimates for $N_A(z)$ for $z < 1250$ nm and for $N_D(z)$ for $z > 1650$ nm. By varying $N_A(z)$ for $1250 < z < 1650$ nm with the aim to recreate the electron potential profile measured with electron holography, we ended up with the concentration profiles shown in Figure 4a. From EBIC and CL measurements on the n side, we had a strong indication that τ_{rec} is rather constant there. With drift-diffusion modelling, we found good agreement between the measured and modelled EBIC with $\tau_{\text{rec}} = 600$ ps in the modelling in the n region. The IV curve of the nanowire diode is predominantly dependent on τ_{rec} in the pn-junction. This fact allowed us to vary τ_{rec} in the $1250 < z < 1650$ nm junction area, without noticeable influence of the τ_{rec} set for $z < 1250$ nm. We found that the same $\tau_{\text{rec}} = 600$ ps as was used for the n region, when used in this junction region, provided good agreement between the measured and modelled IV curves (Figure 2). Lastly, by aiming to recreate the measured EBIC profile in the p segment for $z < 1250$ nm through modelling, we found good agreement when using a graded τ_{rec} (Figure 4b).

However, we must point out that the drift-diffusion model that we developed above for the nanowire does not appear to be absolutely perfect. With that model, we were not able to reproduce the CL intensity profile on the p side (see Figure S7). We leave it as an open question to future studies to investigate this discrepancy. Could the discrepancy for example originate from the effects of radial band-bending due to Fermi-level pinning at the surface of the GaAs nanowire core [40]? Such radial effects cannot be easily included in the 1D model that we used for the nanowire and would need dedicated additional experiments to allow extension of the model to one with both axial and radial dependence.

In conclusion, this work opens the possibility to recreate the internal structure of a nanowire from the information obtained from one or several characterization techniques. The number and type of characterization techniques that are needed are expected to depend on the complexity of the nanowire. Here, we demonstrated how to use modelling aid to

simulate data for the analysis of, e.g., CL, EBIC, IV, and electron holography characterization results, with additional input from the known, nominal nanowire growth design. Such an analysis framework is expected to streamline material and device development in nanowire-based applications.

Supplementary Materials: The following supporting information can be downloaded at <https://www.mdpi.com/article/10.3390/mi15010157/s1>, Figure S1: Measured CL spectra. Figure S2: Doping concentration from CL; Figure S3: Additional modelling of potential profile; Figure S4: Additional modelling of EBIC profile; Figure S5: Additional modelling of EBIC profile; Figure S6: Spatially resolved recombination rate; Figure S7: Modelled CL intensity. Table S1. Summary of the steps and key parameters for the nanowire growth.

Author Contributions: Conceptualization, N.A., G.V. and D.L.; methodology, N.A., E.M.F., J.C.G., G.V. and D.L.; data curation, N.A., E.M.F., J.C.G., G.V. and D.L.; writing—original draft preparation, N.A. and D.L.; writing—review and editing, N.A., E.M.F., J.C.G., G.V. and D.L.; project administration, N.A. and D.L. All authors have read and agreed to the published version of the manuscript.

Funding: This research was partly funded by the Waldemar von Frenckell foundation.

Data Availability Statement: All the necessary data are included in the article.

Acknowledgments: We acknowledge Erik Svensson and Yuxuan Sun for the nanowire growth.

Conflicts of Interest: Authors José Cano Garcia, Giuliano Vesovi and David Lindgren were employed by the company Sol Voltaics AB. The remaining authors declare that the research was conducted in the absence of any commercial or financial relationships that could be construed as a potential conflict of interest.

References

1. Björk, M.T.; Ohlsson, B.J.; Sass, T.; Persson, A.I.; Thelander, C.; Magnusson, M.H.; Deppert, K.; Wallenberg, L.R.; Samuelson, L. One-Dimensional Heterostructures in Semiconductor Nanowhiskers. *Appl. Phys. Lett.* **2002**, *80*, 1058–1060. [\[CrossRef\]](#)
2. Dick, K.A. A Review of Nanowire Growth Promoted by Alloys and Non-Alloying Elements with Emphasis on Au-Assisted III–V Nanowires. *Prog. Cryst. Growth Charact. Mater.* **2008**, *54*, 138–173. [\[CrossRef\]](#)
3. Barrigón, E.; Heurlin, M.; Bi, Z.; Monemar, B.; Samuelson, L. Synthesis and Applications of III–V Nanowires. *Chem. Rev.* **2019**, *119*, 9170–9220. [\[CrossRef\]](#)
4. Yan, R.; Gargas, D.; Yang, P. Nanowire Photonics. *Nat. Photonics* **2009**, *3*, 569–576. [\[CrossRef\]](#)
5. Gudiksen, M.S.; Lauhon, L.J.; Wang, J.; Smith, D.C.; Lieber, C.M. Growth of Nanowire Superlattice Structures for Nanoscale Photonics and Electronics. *Nature* **2002**, *415*, 617–620. [\[CrossRef\]](#) [\[PubMed\]](#)
6. LaPierre, R.R.; Chia, A.C.E.; Gibson, S.J.; Haapamäki, C.M.; Boulanger, J.; Yee, R.; Kuyanov, P.; Zhang, J.; Tajik, N.; Jewell, N.; et al. III–V Nanowire Photovoltaics: Review of Design for High Efficiency. *Phys. Status Solidi RRL—Rapid Res. Lett.* **2013**, *7*, 815–830. [\[CrossRef\]](#)
7. Otnes, G.; Borgström, M.T. Towards High Efficiency Nanowire Solar Cells. *Nano Today* **2017**, *12*, 31–45. [\[CrossRef\]](#)
8. Goktas, N.I.; Wilson, P.; Ghukasyan, A.; Wagner, D.; McNamee, S.; LaPierre, R.R. Nanowires for Energy. *Appl. Phys. Rev.* **2018**, *5*, 041305. [\[CrossRef\]](#)
9. Li, Z.; Tan, H.H.; Jagadish, C.; Fu, L. III–V Semiconductor Single Nanowire Solar Cells: A Review. *Adv. Mater. Technol.* **2018**, *3*, 1800005. [\[CrossRef\]](#)
10. Cui, Y.; Wang, J.; Plissard, S.R.; Cavalli, A.; Vu, T.T.T.; van Veldhoven, R.P.J.; Gao, L.; Trainor, M.; Verheijen, M.A.; Haverkort, J.E.M.; et al. Efficiency Enhancement of InP Nanowire Solar Cells by Surface Cleaning. *Nano Lett.* **2013**, *13*, 4113–4117. [\[CrossRef\]](#)
11. Krogstrup, P.; Jørgensen, H.I.; Heiss, M.; Demichel, O.; Holm, J.V.; Aagesen, M.; Nygard, J.; Fontcuberta i Morral, A. Single-Nanowire Solar Cells beyond the Shockley–Queisser Limit. *Nat. Photonics* **2013**, *7*, 306–310. [\[CrossRef\]](#)
12. Yao, M.; Cong, S.; Arab, S.; Huang, N.; Povinelli, M.L.; Cronin, S.B.; Dapkus, P.D.; Zhou, C. Tandem Solar Cells Using GaAs Nanowires on Si: Design, Fabrication, and Observation of Voltage Addition. *Nano Lett.* **2015**, *15*, 7217–7224. [\[CrossRef\]](#) [\[PubMed\]](#)
13. VJ, L.; Oh, J.; Nayak, A.P.; Katzenmeyer, A.M.; Gilchrist, K.H.; Grego, S.; Kobayashi, N.P.; Wang, S.-Y.; Talin, A.A.; Dhar, N.K.; et al. A Perspective on Nanowire Photodetectors: Current Status, Future Challenges, and Opportunities. *IEEE J. Sel. Top. Quantum Electron.* **2011**, *17*, 1002–1032. [\[CrossRef\]](#)
14. LaPierre, R.R.; Robson, M.; Azizur-Rahman, K.M.; Kuyanov, P. A Review of III–V Nanowire Infrared Photodetectors and Sensors. *J. Phys. Appl. Phys.* **2017**, *50*, 123001. [\[CrossRef\]](#)
15. Mukai, T. Recent Progress in Group-III Nitride Light-Emitting Diodes. *IEEE J. Sel. Top. Quantum Electron.* **2002**, *8*, 264–270. [\[CrossRef\]](#)
16. Sze, S.M.; Li, Y.; Ng, K.K. *Physics of Semiconductor Devices*; John Wiley & Sons: Hoboken, NJ, USA, 2021; ISBN 978-1-119-61800-3.
17. Wallentin, J.; Borgström, M.T. Doping of Semiconductor Nanowires. *J. Mater. Res.* **2011**, *26*, 2142–2156. [\[CrossRef\]](#)

18. Chen, Y.; Kivisaari, P.; Pistol, M.-E.; Anttu, N. Optimization of the Short-Circuit Current in an InP Nanowire Array Solar Cell through Opto-Electronic Modeling. *Nanotechnology* **2016**, *27*, 435404. [[CrossRef](#)]
19. Chen, Y.; Kivisaari, P.; Pistol, M.-E.; Anttu, N. Optimized Efficiency in InP Nanowire Solar Cells with Accurate 1D Analysis. *Nanotechnology* **2017**, *29*, 045401. [[CrossRef](#)]
20. Otnes, G.; Barrigón, E.; Sundvall, C.; Svensson, K.E.; Heurlin, M.; Siefer, G.; Samuelson, L.; Åberg, I.; Borgström, M.T. Understanding InP Nanowire Array Solar Cell Performance by Nanoprobe-Enabled Single Nanowire Measurements. *Nano Lett.* **2018**, *18*, 3038–3046. [[CrossRef](#)]
21. Barrigón, E.; Zhang, Y.; Hrachowina, L.; Otnes, G.; Borgström, M.T. Unravelling Processing Issues of Nanowire-Based Solar Cell Arrays by Use of Electron Beam Induced Current Measurements. *Nano Energy* **2020**, *71*, 104575. [[CrossRef](#)]
22. Gao, Q.; Li, Z.; Li, L.; Vora, K.; Li, Z.; Alabadla, A.; Wang, F.; Guo, Y.; Peng, K.; Wenas, Y.C.; et al. Axial p-n Junction Design and Characterization for InP Nanowire Array Solar Cells. *Prog. Photovolt. Res. Appl.* **2019**, *27*, 237–244. [[CrossRef](#)]
23. Piazza, V.; Wirths, S.; Bologna, N.; Ahmed, A.A.; Bayle, F.; Schmid, H.; Julien, F.; Tchernycheva, M. Nanoscale Analysis of Electrical Junctions in InGaP Nanowires Grown by Template-Assisted Selective Epitaxy. *Appl. Phys. Lett.* **2019**, *114*, 103101. [[CrossRef](#)]
24. Saket, O.; Himwas, C.; Piazza, V.; Bayle, F.; Cattoni, A.; Oehler, F.; Patriarche, G.; Travers, L.; Collin, S.; Julien, F.H.; et al. Nanoscale Electrical Analyses of Axial-Junction GaAsP Nanowires for Solar Cell Applications. *Nanotechnology* **2020**, *31*, 145708. [[CrossRef](#)] [[PubMed](#)]
25. Yang, M.; Darbandi, A.; Watkins, S.P.; Kavanagh, K.L. Geometric Effects on Carrier Collection in Core-Shell Nanowire p-n Junctions. *Nano Futur.* **2021**, *5*, 025007. [[CrossRef](#)]
26. Dastjerdi, M.H.T.; Fiordaliso, E.M.; Leshchenko, E.D.; Akhtari-Zavareh, A.; Kasama, T.; Aagesen, M.; Dubrovskii, V.G.; LaPierre, R.R. Three-Fold Symmetric Doping Mechanism in GaAs Nanowires. *Nano Lett.* **2017**, *17*, 5875–5882. [[CrossRef](#)]
27. Wolf, D.; Hübner, R.; Niermann, T.; Sturm, S.; Prete, P.; Lovergine, N.; Büchner, B.; Lubk, A. Three-Dimensional Composition and Electric Potential Mapping of III-V Core-Multishell Nanowires by Correlative STEM and Holographic Tomography. *Nano Lett.* **2018**, *18*, 4777–4784. [[CrossRef](#)]
28. Pennington, R.S.; Boothroyd, C.B.; Dunin-Borkowski, R.E. Surface Effects on Mean Inner Potentials Studied Using Density Functional Theory. *Ultramicroscopy* **2015**, *159*, 34–45. [[CrossRef](#)] [[PubMed](#)]
29. Barrigón, E.; Hultin, O.; Lindgren, D.; Yadegari, F.; Magnusson, M.H.; Samuelson, L.; Johansson, L.I.M.; Björk, M.T. GaAs Nanowire pn-Junctions Produced by Low-Cost and High-Throughput Aerotaxy. *Nano Lett.* **2018**, *18*, 1088–1092. [[CrossRef](#)]
30. Prete, P.; Wolf, D.; Marzo, F.; Lovergine, N. Nanoscale Spectroscopic Imaging of GaAs-AlGaAs Quantum Well Tube Nanowires: Correlating Luminescence with Nanowire Size and Inner Multishell Structure. *Nanophotonics* **2019**, *8*, 1567–1577. [[CrossRef](#)]
31. Vermeersch, R.; Jacopin, G.; Robin, E.; Pernot, J.; Gayral, B.; Daudin, B. Optical Properties of Ga-Doped AlN Nanowires. *Appl. Phys. Lett.* **2023**, *122*, 091106. [[CrossRef](#)]
32. Åberg, I.; Vescovi, G.; Asoli, D.; Naseem, U.; Gilboy, J.P.; Sundvall, C.; Dahlgren, A.; Svensson, K.E.; Anttu, N.; Björk, M.T.; et al. A GaAs Nanowire Array Solar Cell With 15.3% Efficiency at 1 Sun. *IEEE J. Photovolt.* **2016**, *6*, 185–190. [[CrossRef](#)]
33. Vurgaftman, I.; Meyer, J.R.; Ram-Mohan, L.R. Band Parameters for III-V Compound Semiconductors and Their Alloys. *J. Appl. Phys.* **2001**, *89*, 5815–5875. [[CrossRef](#)]
34. Sotoodeh, M.; Khalid, A.H.; Rezazadeh, A.A. Empirical Low-Field Mobility Model for III-V Compounds Applicable in Device Simulation Codes. *J. Appl. Phys.* **2000**, *87*, 2890–2900. [[CrossRef](#)]
35. Anttu, N. Physics and Design for 20% and 25% Efficiency Nanowire Array Solar Cells. *Nanotechnology* **2018**, *30*, 074002. [[CrossRef](#)] [[PubMed](#)]
36. Kim, W.; Güniat, L.; Fontcuberta i Morral, A.; Piazza, V. Doping Challenges and Pathways to Industrial Scalability of III-V Nanowire Arrays. *Appl. Phys. Rev.* **2021**, *8*, 011304. [[CrossRef](#)]
37. Hudait, M.K.; Modak, P.; Hardikar, S.; Krupanidhi, S.B. Zn Incorporation and Band Gap Shrinkage in p-Type GaAs. *J. Appl. Phys.* **1997**, *82*, 4931–4937. [[CrossRef](#)]
38. Arab, S.; Yao, M.; Zhou, C.; Daniel Dapkus, P.; Cronin, S.B. Doping Concentration Dependence of the Photoluminescence Spectra of n-Type GaAs Nanowires. *Appl. Phys. Lett.* **2016**, *108*, 182106. [[CrossRef](#)]
39. Cusano, D.A. Radiative Recombination from GaAs Directly Excited by Electron Beams. *Solid State Commun.* **1964**, *2*, 353–358. [[CrossRef](#)]
40. Yablonovitch, E.; Skromme, B.J.; Bhat, R.; Harbison, J.P.; Gmitter, T.J. Band Bending, Fermi Level Pinning, and Surface Fixed Charge on Chemically Prepared GaAs Surfaces. *Appl. Phys. Lett.* **1989**, *54*, 555–557. [[CrossRef](#)]

Disclaimer/Publisher’s Note: The statements, opinions and data contained in all publications are solely those of the individual author(s) and contributor(s) and not of MDPI and/or the editor(s). MDPI and/or the editor(s) disclaim responsibility for any injury to people or property resulting from any ideas, methods, instructions or products referred to in the content.